

CONTRASTING GALAXY FORMATION FROM QUANTUM WAVE DARK MATTER, ψ DM, WITH Λ CDM, USING PLANCK AND HUBBLE DATA

HSI-YU SCHIVE¹, TZIHONG CHIUH^{1,2,3}, TOM BROADHURST^{4,5}, & KUAN-WEI HUANG¹

Draft version October 8, 2018

ABSTRACT

The newly established luminosity functions of high- z galaxies at $4 \lesssim z \lesssim 10$ can provide a stringent check on dark matter models that aim to explain the core properties of dwarf galaxies. The cores of dwarf spheroidal galaxies are understood to be too large to be accounted for by free streaming of warm dark matter without overly suppressing the formation of such galaxies. Here we demonstrate with cosmological simulations that wave dark matter, ψ DM, appropriate for light bosons such as axions, does not suffer this problem, given a boson mass of $m_\psi \geq 1.2 \times 10^{-22}$ eV (2σ). In this case, the halo mass function is suppressed below $\sim 10^{10} M_\odot$ at a level that is consistent with the high- z luminosity functions, while simultaneously generating the kpc-scale cores in dwarf galaxies arising from the solitonic ground state in ψ DM. We demonstrate that the reionization history in this scenario is consistent with the Thomson optical depth recently reported by Planck, assuming a reasonable ionizing photon production rate. We predict that the luminosity function should turn over slowly around an intrinsic UV luminosity of $M_{UV} \gtrsim -16$ at $z \gtrsim 4$. We also show that for galaxies magnified $>10\times$ in the Hubble Frontier Fields, ψ DM predicts an order of magnitude fewer detections than cold dark matter at $z \gtrsim 10$ down to $M_{UV} \sim -15$, allowing us to distinguish between these very different interpretations for the observed coldness of dark matter.

Subject headings: cosmology: theory – dark ages, reionization, first stars – dark matter – galaxies: abundances – galaxies: evolution – galaxies: high-redshift

1. INTRODUCTION

The transitional stage when density perturbations first collapse to become galaxies is now being reached with data of unprecedented depth. New polarization measurements with the Planck satellite indicate an optical depth of only $\tau_e = 0.066 \pm 0.016$, for electron scattering of the cosmic microwave background (CMB), which translates into an approximate instantaneous reionization redshift of $z \sim 8.8_{-1.4}^{+1.7}$ (Planck Collaboration et al. 2015).

This may be compared with the ionization state of hydrogen absorption lines revealed by distant, bright quasi-stellar objects (QSOs) and gamma-ray bursts (GRBs), which has demonstrated that inter-galactic hydrogen has remained highly ionized since at least $z \sim 6$. Beyond which evidence of a patchy opacity is claimed in some QSO and GRB spectra (Chornock et al. 2014; Melandri et al. 2015; Becker et al. 2015) with a small mean enhancement in the average neutral fraction by $z = 6.5$ (Hartoog et al. 2014). The forest at $z > 6.5$ is not yet measured with any bright source, but a large jump in neutral hydrogen fraction may be implied in the range $6.5 < z < 7.0$ from the statistical absence of strong Lyman- α emission from the most distant galaxies amenable to spectroscopy (Pentericci et al. 2014; Stark

et al. 2015). Exceptions have been found with strong Lyman- α emission at $z \sim 7.7$ (Oesch et al. 2015), and also the currently highest redshift galaxy established by spectroscopy at $z \sim 8.7$ (Zitrin et al. 2015). A relatively sharp reionization transition is considered likely if galaxies are the dominant source of reionization, based on advanced hybrid techniques (Mesinger et al. 2015) which justifies the instantaneous reionization redshift approximation (Dijkstra 2014; Mitra et al. 2015). More detailed 3D modeling of this transition remains very challenging when incorporating all relevant processes which may affect ultraviolet (UV) ionization (e.g., Springel & Hernquist 2003; Bromm & Yoshida 2011; Wise et al. 2014), including early galactic outflows (e.g., Frye et al. 2002) and their feedback effects (e.g., Scannapieco & Broadhurst 2001; Pieri et al. 2007; Booth et al. 2012).

This relatively low value of τ_e implies that galaxies may not be expected to be found in abundance at redshifts much higher than $z \sim 9$. Indeed beyond this redshift only a handful of galaxies are claimed in the deepest fields, among which the current most distant galaxy has $z \sim 10.7$, which is discovered in the CLASH program and is highly magnified by gravitational lensing (Coe et al. 2013). Two other reliably estimated high- z galaxies are also known behind the new, highly magnifying Hubble Frontier Field (HFF) clusters at $z \sim 9.6$ (Zheng et al. 2012) and $z \sim 9.8$ (Zitrin et al. 2014). Nothing beyond this has been found in HFF so far, despite the high magnifications by these clusters (Zitrin & Broadhurst 2009; Lam et al. 2014; Diego et al. 2015) and the great depth of these images in the near infrared, with their potential to detect even higher redshift galaxies to a photometric limit of $z \sim 11.5$ (Coe et al. 2015).

The UV luminosity function (LF) of distant galaxies

hyschive@ntu.edu.tw

¹ Department of Physics, National Taiwan University, 10617 Taipei, Taiwan

² Institute of Astrophysics, National Taiwan University, 10617 Taipei, Taiwan

³ Center for Theoretical Sciences, National Taiwan University, 10617 Taipei, Taiwan

⁴ Department of Theoretical Physics, University of the Basque Country UPV/EHU, E-48080 Bilbao, Spain

⁵ Ikerbasque, Basque Foundation for Science, E-48011 Bilbao, Spain

is now well constructed at $z \sim 4 - 10$ relying mainly on dropout galaxies detached in deep field searches (e.g., Bouwens et al. 2015b, hereafter B15b). The LF is seen to steadily evolve to low number densities of high redshift galaxies and to steepen at the faint-end slope as it does so (B15b). Evolution is also seen in terms of the mean sizes of dropout galaxies which steadily decrease with increasing redshift (Bouwens et al. 2003; Holwerda et al. 2015). Currently, the behavior of the UV luminosity density at $z > 8$ is hotly debated with evidence of an accelerated decline at $z > 8$ by B15b but with a counter claim by McLeod et al. (2015) for the HFF with a reliance on parametric lens modeling. This latter claim is at odds with Coe et al. (2015) who provide some evidence of a deficit at high redshifts for the HFF, based on the first two completed clusters. Of course in this $z \gtrsim 9$ redshift range data is restricted to fewer detections in only infrared passbands lying close to magnitude limits, so that crucial conclusions regarding galaxy formation are still uncertain.

In this paper, we examine the high-redshift galaxy formation in the context of a wave dark matter model, known as ψ DM (Schive et al. 2014a, hereafter SCB14a) or *fuzzy* dark matter (Hu et al. 2000). In this scenario, dark matter is assumed to be composed of extremely light bosons, such as axion-like particles proposed by string theory (Arvanitaki et al. 2010) or non-QCD axions (Chiueh 2014). They are non-thermally generated and can be described by a single coherent wave function (Turner 1983; Goodman 2000; Böhmer & Harko 2007; Sikivie & Yang 2009; Davidson 2015; Guth et al. 2015). When self-interaction is negligible, the evolution of ψ DM is governed by the Schrödinger-Poisson equation (Ruffini & Bonazzola 1969; Seidel & Suen 1990; Widrow & Kaiser 1993; Hu et al. 2000; Woo & Chiueh 2009; Schive et al. 2014b), with a single free parameter, m_ψ , the dark matter particle mass.

The most prominent feature in ψ DM is that the uncertainty principle counters gravity below a Jeans scale, resulting in a suppression of halos below $\sim 10^{10} M_\odot$ and a flat density profile within $\sim 0.1 - 1.0$ kpc of the centers of galaxies, assuming $m_{22} \sim 1.0$ where $m_{22} = m_\psi / 10^{-22}$ eV (Khlopov et al. 1985; Peebles 2000; Hu et al. 2000; Matos & Arturo Ureña-López 2001; Lee & Lim 2010; Marsh & Ferreira 2010; Schive et al. 2014a). This boson mass scale can naturally arise in a non-QCD axion model (Chiueh 2014), lending support for the very light boson. The ψ DM model has become a viable dark matter candidate (e.g., Woo & Chiueh 2009; Mielke & Pérez 2009; Chavannis 2011; Suárez & Matos 2011; Robles & Matos 2012; Marsh & Silk 2014; Rindler-Daller & Shapiro 2014; Lora & Magaña 2014; Bray & Goetz 2014; Suárez et al. 2014; Bozek et al. 2015; Marsh & Pop 2015; Martinez-Medina et al. 2015; Guzmán & Lora-Clavijo 2015; Madarassy & Toth 2015; Harko & Lobo 2015), especially given the increasingly strict limits of non-detections of the weakly interacting massive particles (WIMPs) in the standard cold dark matter (CDM, Akerib et al. 2014). Various observable properties of this model have been proposed (Amendola & Barbieri 2006; Arvanitaki & Dubovsky 2011; Schive et al. 2014a,b; Khmelnitsky & Rubakov 2014; Hlozek et al. 2015; Van Tilburg et al. 2015; Stadnik & Flambaum 2015).

The first high-resolution cosmological simulations for

the ψ DM model have recently generated exciting results (SCB14a). We have directly demonstrated that indeed the large-scale structure of ψ DM is statistically indistinguishable from CDM, but differs radically on small scales, where ψ DM halos form central solitonic cores surrounded by fine-scale, large-amplitude granular textures. By applying a Jeans analysis to the stellar phase-space distribution in the Fornax dwarf spheroidal (dSph) galaxy, which is known to have a distinct core (e.g., Amorisco et al. 2013), we determine $m_{22} = 0.8 \pm 0.2$ (1σ), thereby providing the crucial normalization of this model (SCB14a).

From our numerical simulations and theoretical arguments based on the scaling symmetry of the Schrödinger-Poisson equation and the uncertainty principle, we subsequently derived a unique core-halo mass relation in ψ DM (Schive et al. 2014b, hereafter S14b), $M_c \propto (1+z)^{1/2} M_h^{1/3}$, where M_c and M_h are the core mass and halo mass, respectively, and z is redshift. This relation predicts that massive galaxies with $M_h \sim 10^{12} M_\odot$ at $z \sim 8$ will have compact solitons of $M_c \sim 10^9 M_\odot$ within ~ 60 pc. Our simulations show that these dense solitonic cores form promptly after halo collapse, and thus may help to explain the early onset of QSO activity (Trakhtenbrot et al. 2015) by acting as a massive focus for gas accretion.

Another key prediction of ψ DM is that galaxy formation is *delayed* relative to CDM because of the inherent Jeans scale. The preliminary results of SCB14a showed that the first galaxies form at $z \sim 13$ with $M_h \sim 10^9 - 10^{10} M_\odot$, assuming $m_{22} \sim 1.0$ fixed by the scale of dSph galaxy cores as described above. Halos below $\sim 10^9 M_\odot$ are significantly suppressed. We stress that the particle mass, m_{22} , is the only free parameter here assuming that the dark matter is made entirely of ψ DM (see Marsh & Silk 2014 for a mixed CDM and ψ DM model). The smaller the m_{22} , the greater the difference between CDM and ψ DM. Here we aim to establish whether a similar particle mass ($m_{22} \sim 1.0$) can satisfy both the observed properties of dSph galaxies and the constraints from high- z observations, such as galaxy counts, reionization history, and Lyman- α forest, although some tension seems to exist (Bozek et al. 2015). It is a well known issue for warm dark matter (WDM), usually termed as the *Catch 22* problem (Macciò et al. 2012), where the kpc-scale cores in dSph galaxies require too small a WDM particle mass that is in contradiction with high- z observations (Schneider et al. 2014; Schultz et al. 2014; Lovell et al. 2014). Since the relation between core radius and power spectrum suppression are different in ψ DM and WDM (Hu et al. 2000; Schive et al. 2014b; Marsh & Pop 2015), in this work we examine in detail whether ψ DM is clear of this serious problem facing WDM.

In this paper we conduct cosmological simulations to study the evolution of halo mass function (MF) in the ψ DM scenario, and connect it to the recently established galaxy UV LF at $4 \lesssim z \lesssim 10$. We explore the results of different ψ DM particle masses ranging from $m_{22} = 0.8$ to 3.2. We predict the evolution of LF beyond the current observational limit as a future test to distinguish between CDM and ψ DM. We also perform analytic calculations to study the reionization history in this context,

and compare it to the Thomson optical depth recently reported by Planck. All magnitudes in this paper are quoted in the AB system (M_{AB} , Oke & Gunn 1983).

The paper is structured as follows. In Section 2 we describe our simulation setup, including initial conditions and simulation characteristics. We show the ψ DM halo mass function in Section 3, and compare it with observations in Section 4. Finally, we discuss and summarize our results in Section 5.

2. SIMULATIONS

In this section, we describe the initial power spectra and other characteristics of our simulations for the study of the evolution of the ψ DM halo MF at high redshifts.

2.1. Initial Power Spectra

The suppression of ψ DM linear density power spectrum relative to CDM can be expressed as

$$P_{\psi\text{DM}}(k, z) = T_{\psi\text{DM}}^2(k, z) P_{\text{CDM}}(k, z), \quad (1)$$

where P denotes the power spectrum and $T_{\psi\text{DM}}$ is the ψ DM transfer function (strictly speaking it is the ratio between the transfer functions of ψ DM and CDM). In general $T_{\psi\text{DM}}$ is both redshift- and scale-dependent since the balance between gravity and quantum pressure introduces a redshift-dependent Jeans scale, $k_J(z)$, below which the structures cannot grow. However, for the particle masses, redshift range, and halo masses of interest in this work ($m_{22} \sim 1$, $z \sim 4-10$, $M_h \gtrsim 1 \times 10^9 M_\odot$), $T_{\psi\text{DM}}$ can be approximated as redshift-independent, as we demonstrate below.

The redshift evolution of ψ DM density perturbations during the matter-dominated epoch can be described analytically by (Woo & Chiueh 2009)

$$\rho_k(k, z) = A(k) \frac{3 \cos \theta - \theta^2 \cos \theta + 3\theta \sin \theta}{\theta^2}, \quad (2)$$

where ρ_k is the spatial Fourier component of the comoving density perturbations, $A(k)$ is the normalization constant, $\theta(k, z) = \hbar k^2 \sqrt{1+z}/m_\psi H_0 \sqrt{\Omega_{m0}}$, H_0 is the present Hubble parameter, and Ω_{m0} is the present matter density parameter. Setting $\theta^2 = 6$ gives the Jeans scale,

$$k_J(z) \approx 69.1 m_{22}^{1/2} \left(\frac{\Omega_{m0} h^2}{0.14} \right)^{1/4} (1+z)^{-1/4} \text{Mpc}^{-1}, \quad (3)$$

where h is the dimensionless Hubble constant. For $k \ll k_J$, we have $\rho_k \propto (1+z)^{-1}$, and thus ψ DM grows like CDM; while for $k \gg k_J$ the perturbations oscillate as $\rho_k \propto \cos \theta$. Note that $k_J(z)$ increases slowly with time, and hence an oscillating mode may become a growing mode at lower redshifts, but not vice versa.

To quantify the difference in growth rate between ψ DM and CDM density perturbations during a given redshift interval, $z_{\text{start}} \geq z \geq z_{\text{end}}$, we define

$$\xi(k) = \frac{\rho_k(k, z_{\text{end}})/\rho_k(k, z_{\text{start}})}{\rho_k(k_0, z_{\text{end}})/\rho_k(k_0, z_{\text{start}})}, \quad (4)$$

with $k_0 \ll k_J$ so that the denominator represents the growth in CDM. For $k \ll k_J$, ψ DM grows like CDM, and thus $\xi \sim 1$. For $k \sim k_J$, quantum pressure starts to

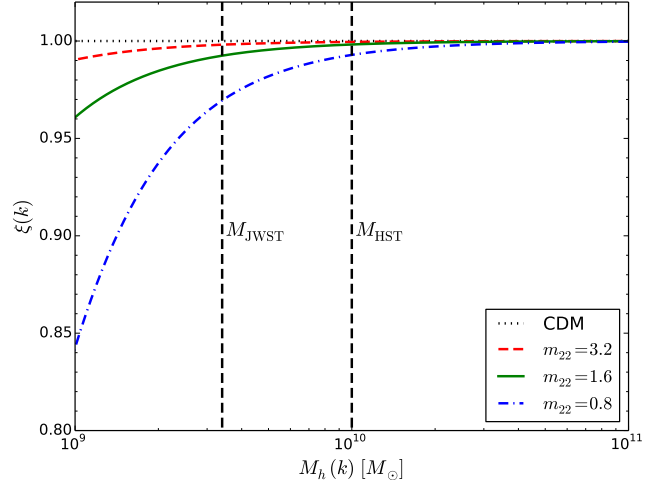


FIG. 1.— Growth rate ratio between ψ DM and CDM density perturbations (Eq. [4]) during $30 \geq z \geq 4$. Vertical dashed lines highlight the mass of the faintest galaxies currently observed by HST at $z \gtrsim 4$ (M_{HST}) and that expected for JWST assuming a limiting absolute magnitude of $M_{\text{UV}} = -15$ at $z = 6$ (M_{JWST}). Here we have adopted the mass-luminosity relation described in Section 4.2.1. Note that even for $m_{22} = 0.8$ the growth rate ratios still reach $\xi \sim 0.99$ at $M_h = M_{\text{HST}}$ and $\xi \sim 0.97$ at $M_h = M_{\text{JWST}}$, indicating that the additional suppression of ψ DM halos above M_{JWST} during this redshift interval of interest is almost negligible (see text for details).

counter gravity and leads to $\xi < 1$, indicative of ‘additional’ suppression of ψ DM halos during this epoch.

Figure 1 shows $\xi(k)$ for various ψ DM particle masses. We take $z_{\text{start}} = 30$ so that the ψ DM density perturbations are still in the linear regime, and $z_{\text{end}} = 4$ to bracket the redshifts of interest in this work. We convert the wavenumber to the halo virial mass via $M_h = 4\pi(\pi/k)^3 \rho_m/3$, where ρ_m is the comoving matter density. A relatively large deviation from CDM is found at the low-mass end for a smaller particle mass because of the corresponding longer Jeans wavelength. However, note that the faintest galaxies currently observed by the Hubble Space Telescope (HST) at $z \gtrsim 4$ have $M_h \sim 10^{10} M_\odot$ (see Sec. 4.2.1 for the mass-luminosity relation adopted), at which $\xi \sim 0.99$ for $m_{22} = 0.8$. Even for the James Webb Space Telescope (JWST, Gardner et al. 2006) assuming a limiting absolute magnitude of $M_{\text{UV}} \sim -15$ at $z \sim 6$, we still have $\xi \sim 0.97$ for $m_{22} = 0.8$. It demonstrates that *for the particle masses, redshifts, and halo masses of interest when comparing with current and forthcoming observations, (i) the growth rate of linear density power spectra in CDM and ψ DM are similar, and (ii) the ψ DM transfer function $T_{\psi\text{DM}}$ can be well approximated as redshift-independent.* This is primarily due to that the Jeans mass at $z = 30$ for $m_{22} = 0.8$ is $\sim 2.7 \times 10^8 M_\odot$, well below the observational limits. Note, also, that the smallest halos resolved in our simulations have $M_h \sim 3 \times 10^8 M_\odot$, close to the Jeans mass and hence $\xi \sim 0.52$ for $m_{22} = 0.8$. Therefore the halo MF at the low-mass end may be, in this sense, slightly underestimated in our simulations.

The ψ DM transfer function at $z = 0$ is given by (Hu et al. 2000)

$$T_{\psi\text{DM}} \approx \frac{\cos x^3}{1+x^8}, \quad x = 1.61 m_{22}^{1/18} \frac{k}{k_{J,\text{eq}}}, \quad (5)$$

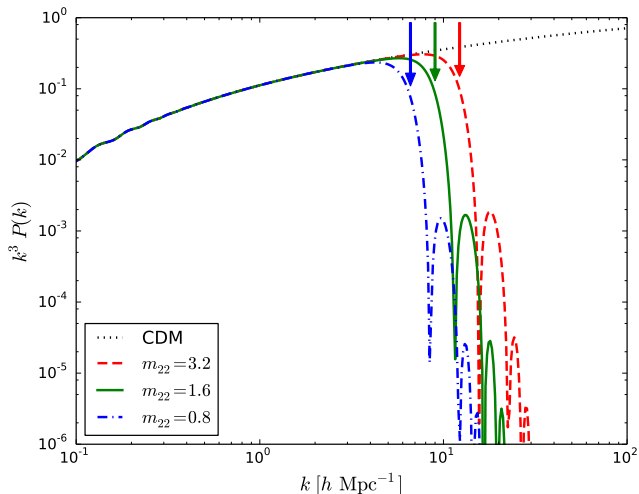


FIG. 2.— Linear matter power spectra at $z = 30$ in CDM and ψ DM. ψ DM power spectra are obtained using Equations (1) and (5), where we have assumed that $T_{\psi\text{DM}}$ can be well approximated as redshift-independent during $30 \geq z \geq 0$ (see Fig. 1). Note that the smaller the particle mass, the stronger the suppression at the high- k end. Arrows indicate the half-mode wavenumbers, $k_{1/2}$ (Eq. [6]), where the power spectra drop by a factor of four compared to CDM.

which is assumed to be redshift-independent relevant for the redshifts and wavenumbers of interest. Here $k_{J,\text{eq}} = 9 m_{22}^{1/2} \text{Mpc}^{-1}$ is the Jeans wavenumber at matter-radiation equality. Figure 2 presents the linear matter power spectra at $z = 30$, which exhibit sharp breaks at $k \sim k_{J,\text{eq}}$ and strong oscillations for $k > k_{J,\text{eq}}$. We can also define the characteristic scale to be the ‘half-mode’ scale, $k_{1/2}$, where $T_{\psi\text{DM}}(k_{1/2}) = 1/2$. Equation (5) then gives

$$k_{1/2} \approx 5.1 m_{22}^{4/9} \text{Mpc}^{-1}, \quad M_{1/2} \approx 3.8 \times 10^{10} m_{22}^{-4/3} M_{\odot}, \quad (6)$$

where $M_{1/2} = 4\pi(\pi/k_{1/2})^3 \rho_m/3$ is the characteristic halo mass where a noticeable difference between ψ DM and CDM MFs is expected. Note that the strong suppression at $k \sim k_{J,\text{eq}}$ shown by Equation (5) is mainly determined during the radiation-dominated epoch (Hu et al. 2000), and thus cannot be solely explained by Equation (2) which is only valid during the matter-dominated epoch.

2.2. Simulation Characteristics

Bona-fide ψ DM simulations involve solving the Schrödinger-Poisson equation, which is extremely challenging owing to its wave nature. The matter wave dispersion relation, $\omega \propto \lambda^{-2} \propto v^2$, where ω , λ , v are the angular frequency, wavelength, and velocity, respectively, indicates that exceptionally high spatial and temporal resolutions are required for resolving the wave functions of high-velocity flows throughout a simulation box (SCB14a). Numerically, we find that a comoving spatial resolution as high as $\sim 1 h^{-1} \text{kpc}$ is required to properly resolve a flow with a moderate peculiar velocity of $\sim 100 \text{kms}^{-1}$ at $z \sim 13$. Otherwise we find the flow velocity can be underestimated, leading to lower mass accretion rate and underestimation of MF. In the extreme case, a ψ DM simulation in a $30 h^{-1} \text{Mpc}$ box with a uniform $1 h^{-1} \text{kpc}$ spatial resolution will consume ~ 400 terabytes of memory, which is impractical in any mod-

ern supercomputer. As a result, even the state-of-the-art ψ DM simulations currently can only fully resolve a comoving box as small as $1.4 h^{-1} \text{Mpc}$ at $z = 0$ (SCB14a).

In this paper we mainly focus on determining the ψ DM halo MF above $\sim 1 \times 10^9 M_{\odot}$ at $z \geq 4$, for which most halos are isolated and thus insensitive to the subtle differences between CDM and ψ DM halos. Nor are we interested here in the complex wave nature of the internal density profiles of the halos, which we have already established in our previous wave-based simulations (SCB14a, S14b). As we demonstrated in the previous subsection, the growth rates of density perturbations in CDM and ψ DM are similar in the context of this work and differ mainly in their initial amplitudes. Moreover, S14b verified that CDM and ψ DM halos have similar virial masses during the same collapse process. All these facts indicate that, *for the purpose of this study, it is appropriate to use simulations of collisionless particles with ψ DM initial power spectra to approximate real ψ DM simulations.* This is the approach adopted in this work, which is essentially the same as most WDM simulations where initial thermal velocity are ignored. Real ψ DM simulations for supporting these arguments, solving either wave function directly or an alternative fluid-like form (e.g., Mocz & Succi 2015; Marsh 2015), are for future work.

All simulations are run from $z = 100$ to 4. Since the linear power spectra relevant for this study do not change in shape after $z = 30$, we can directly apply Equation (5) to obtain the ψ DM power spectra at $z = 30$ (see Fig. 2). To capture the rare non-Gaussian peaks, which are the seeds of first galaxies, due to nonlinearity set in as early as $z \sim 30$, we then extrapolate the $z = 30$ spectra to $z = 100$ for which the amplitude is ~ 3.3 times smaller to ensure all perturbations are Gaussian. By doing so, the simulations of collisionless particles preserve the shape of the spectra from $z = 100$ to $z = 30$ but allow for the development of rare non-Gaussian peaks.

We perform simulations with the GADGET-2 N-body code (Springel 2005). We adopt the CAMB package (Lewis et al. 2000) to generate the CDM transfer function, and construct initial conditions for simulations using the MUSIC code (Hahn & Abel 2011). We adopt the cosmological parameters consistent with the WMAP9 data (Hinshaw et al. 2013): $\Omega_{m0} = 0.284$, $\Omega_{\Lambda0} = 0.716$, $h = 0.696$, $\sigma_8 = 0.818$, and $n_s = 0.962$. We choose three different simulation configurations with $(L, N) = (15 h^{-1} \text{Mpc}, 512^3)$, $(15 h^{-1} \text{Mpc}, 1024^3)$, and $(30 h^{-1} \text{Mpc}, 1024^3)$, where L is the comoving box size and N is the total number of simulation particles. The corresponding simulation particle masses are $\sim 2.8 \times 10^6 M_{\odot}$ and $\sim 3.6 \times 10^5 M_{\odot}$ for the lower and higher mass-resolution simulations, respectively. For each simulation configuration, we run four different dark matter models: CDM, ψ DM with $m_{22} = 0.8, 1.6, \text{ and } 3.2$.

3. MASS FUNCTION

The main aim of our simulations is to determine the halo MF as a function of ψ DM particle mass. Intuitively, a sharp break in the initial power spectrum should translate into a strong suppression of low-mass halos, as verified by the Sheth-Tormen (Sheth & Tormen 1999, hereafter ST99) MF with a sharp k -space window function (Schneider et al. 2013). However, it is well known that the particle simulations with an initial power spectrum

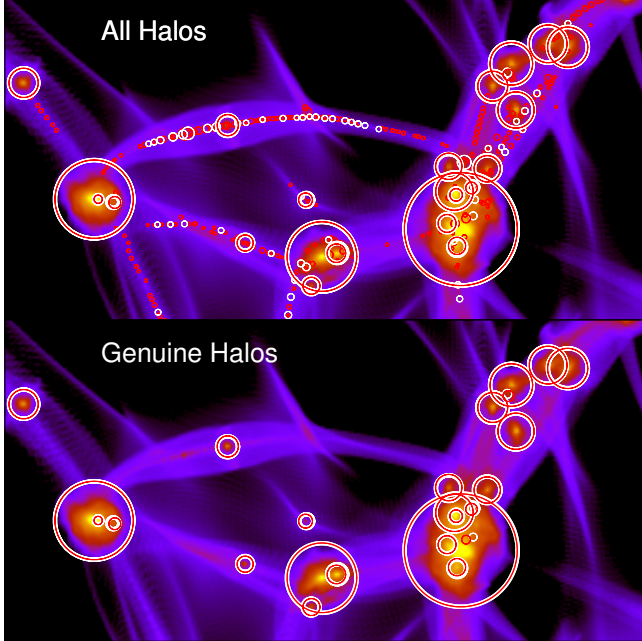


FIG. 3.— Density field at $z = 4$ for ψ DM simulations with $m_{22} = 1.6$ in a $15 h^{-1}$ Mpc box. Each image displays a projected field for a $3 h^{-1}$ Mpc thick slab with a size of $2.70 \times 1.35 h^{-1}$ Mpc. White and red circles show halos more massive than $2 \times 10^7 M_{\odot}$ in the 512^3 and 1024^3 simulations, respectively, where the radii of circles equal the halos’ virial radii. The most massive halo has a mass of $\sim 1 \times 10^{12} M_{\odot}$. The upper panel shows both genuine and spurious halos, while the lower panel only shows genuine halos. Suspicious low-mass halos, which are mostly confined along filaments and have no clear counterparts in the 512^3 and 1024^3 runs, are identified as spurious, while only massive halos with a good match between low- and high-resolution simulations are regarded as genuine.

cut-off suffer from the formation of spurious halos, especially at low masses (Wang & White 2007; Angulo et al. 2013; Schneider et al. 2013).

These spurious halos are caused by artificial fragmentation due to numerical artifacts (Wang & White 2007), and are mostly confined along cosmic filaments (see Fig. 3, upper panel). They outnumber genuine halos below a characteristic mass, which linearly depends on the mean interparticle separation (Wang & White 2007), resulting in a prominent upturn in MF at the low-mass end (see Fig. 4, open symbols). We define ‘protohalo’ as the initial particle positions of an identified halo. Lovell et al. (2014) showed that the protohalos of genuine and spurious halos have distinct features. Genuine protohalos are spheroidal and have a good match between low- and high-resolution simulations, while spurious protohalos have disc-like shapes and their masses and positions are sensitive to the simulation resolution, and thus do not have clear counterparts in simulations with different resolution. To identify and remove these artificial halos, we thus adopt a similar approach suggested by Lovell et al. (2014) based on the shape of the protohalos and the spatial overlap between low-resolution protohalos and their high-resolution counterparts. See Appendix A for a more detailed description of the algorithms adopted.

Figure 4 shows the halo MF obtained in our simulations. For comparison, we show both the ‘original’ MF (containing both genuine and spurious halos) in the $30 h^{-1}$ Mpc simulations with 1024^3 particles, and the ‘genuine’ MF (with spurious halos removed) in the

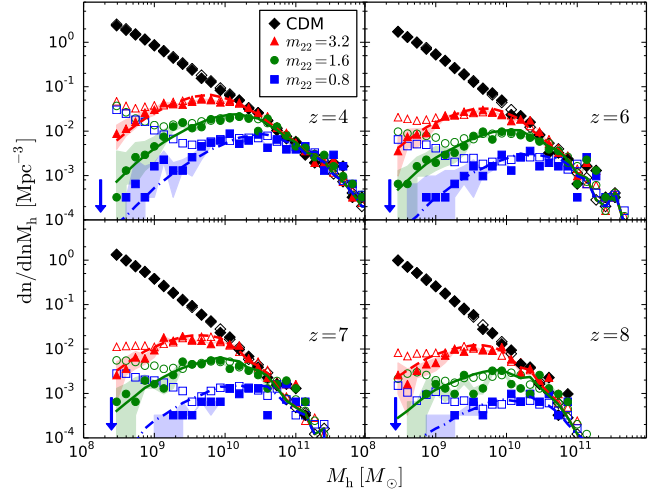


FIG. 4.— Halo mass function (MF) in logarithmic mass bins. The open symbols represent the original MF containing both genuine and spurious halos in the $30 h^{-1}$ Mpc simulations with 1024^3 particles, and the filled symbols show the genuine MF with spurious halos removed in the $15 h^{-1}$ Mpc simulations using 512^3 and 1024^3 particles for estimating the spatial overlap factor. The spurious halos outnumber genuine halos at low masses, resulting in an unphysical upturn at the low-mass end of the original MF, especially for lower m_{22} . By contrast, the genuine MF reveals a prominent drop at the low-mass end, as anticipated and seen in our high-resolution wave-based simulations, reported earlier. The shaded regions indicate the uncertainties of genuine MF by varying S_{cut} and O_{cut} by $\pm 20\%$ (see Appendix A). Various lines show the analytic form, Equation (7), which fit the simulation results well. Arrows mark the minimum ψ DM halo masses proposed by S14b for $m_{22} = 0.8$.

$15 h^{-1}$ Mpc simulations using 512^3 and 1024^3 particles for estimating the spatial overlap factor. The original ψ DM MF shows a prominent upturn at the low-mass end due to the contamination from spurious halos, especially for lower m_{22} . By contrast, the genuine ψ DM MF features a clear drop at low masses for all redshifts and particle masses, apparently different from CDM and in agreement with the expectation from a sharp break in the ψ DM initial power spectra. It is also consistent with the minimum ψ DM halo mass at $z \gtrsim 1$ proposed by S14b, $M_{\text{min}} = 3.7 \times 10^7 m_{22}^{-3/2} (1+z)^{3/4} M_{\odot}$ (indicated by arrows in Fig. 4 for $m_{22} = 0.8$). On the other hand, the original and genuine CDM MFs are almost indistinguishable, which is no surprise since we assume most CDM halos are genuine when calibrating the thresholds for removing spurious halos.

The shaded regions in Figure 4 indicate the uncertainties of genuine ψ DM MF by varying S_{cut} and O_{cut} by $\pm 20\%$ (see Appendix A). It shows that the finding of strong suppression of low-mass halos in ψ DM is reliable, but the exact slope at the low-mass end is still uncertain. In the high-mass end ($M_h \gtrsim 10^{11} M_{\odot}$) the original MF is smoother because of a larger simulation box. Note, however, that in the intermediate mass range ($M_h \sim 3 \times 10^9 - 1 \times 10^{11} M_{\odot}$) the original and genuine MFs are reasonably consistent with each other, suggesting that in this mass range (i) most halos are genuine and (ii) a $15 h^{-1}$ Mpc simulation box is sufficient to obtain an accurate MF. These results make the ψ DM MF obtained in this work more robust for the purpose of comparing with observations.

As shown in Figure 4, the genuine ψ DM MF can be well fitted by the following analytic form:

$$\left. \frac{dn}{dM_h} \right|_{\psi\text{DM}}(M_h, z) = \left. \frac{dn}{dM_h} \right|_{\text{CDM}}(M_h, z) \left[1 + \left(\frac{M_h}{M_0} \right)^{-1.1} \right]^{-2.2} \quad (7)$$

where dn/dM_h is the halo MF and $M_0 = 1.6 \times 10^{10} m_{22}^{-4/3} M_\odot$ is the characteristic mass below which MF starts to drop noticeably. CDM corresponds to $m_{22} \rightarrow \infty$. The facts that M_0 has the same particle mass dependence as the half-mode mass $M_{1/2}$ (Eq. [6]) and ψ DM MF drops by a factor of two relative to CDM at $M_h \sim M_{1/2}$ reinforce our simulation results. Also note that the suppression term, $(1 + (M_h/M_0)^{-1.1})^{-2.2}$, is redshift-independent. It is expected since in this work the effect of quantum pressure is taken into account only for the initial conditions. In detail for ψ DM the suppression of low-mass halos will be redshift-dependent, but the characteristic mass M_0 is still expected to be almost redshift-independent since it is mainly determined during the radiation-dominated epoch (Hu et al. 2000). We emphasize that the faintest galaxies currently observed at $z \gtrsim 4$ have $M_h \sim 10^{10} M_\odot$ (see Fig. 5 and Sec. 4.2.1), which is close to M_0 and hence is insensitive to the uncertainties at low masses of MF ($M_h \lesssim 10^9 M_\odot$) caused by neglecting the dynamical effect of quantum pressure and the removal of spurious halos. Equation (7) thus provides a very convenient comparison between models and observations (see next section).

4. PREDICTIONS VS OBSERVATIONS

The rest-frame UV LF at high redshifts have become increasingly well defined and hence useful for testing a range of dark matter models in detail. The physical mechanisms assumed to solve the small-scale issues of CDM in the Local Group will likely suppress the formation of faint galaxies at high redshifts as well, so that it is important to examine whether too few high- z galaxies are created and with a too small Thomson optical depth to CMB. This is a well-known issue for WDM, usually termed as the *Catch 22* problem (Macciò et al. 2012). In this section we examine the level of consistency in the case of ψ DM.

4.1. Cumulative Mass Function

The cumulative galaxy number density, defined as the total number of galaxies per unit comoving volume at a given redshift, can be converted into a lower limit of m_{22} , below which the ψ DM MF cannot account for the observed counts of galaxies. To relate the UV magnitude M_{UV} of a galaxy to its corresponding halo mass, we first adopt the abundance matching technique (Vale & Ostriker 2004) which equates the cumulative UV LF, $\Psi(<M_{\text{UV}}, z)$, to the cumulative halo MF, $n(>M_h, z)$. An alternative approach using the conditional LF formalism will be discussed later.

For a given LF, one can apply abundance matching to either ψ DM MF with the particle masses of interest (Bozek et al. 2015) or CDM MF (Schultz et al. 2014), both of which have advantages and disadvantages. The former provides a model-independent constraint since it simply checks whether the total numbers of ψ DM

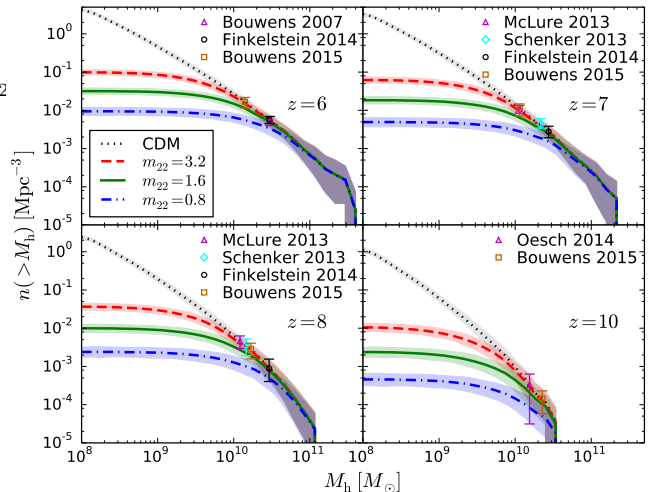


FIG. 5.— Cumulative mass function (MF) at $z = 6 - 10$. The shaded regions indicate the 2σ uncertainties. Error bars show the observational constraints (2σ at $z = 6 - 8$ and 1σ at $z = 10$), which match the CDM MFs perfectly simply because they are derived from applying abundance matching to the CDM MFs. Note that in this approach the faintest galaxies currently observed at $z \sim 4 - 10$ all have $M_h \sim 10^{10} M_\odot$. ψ DM cumulative MFs have finite upper limits due to the strong suppression of low-mass halos. $m_{22} = 3.2$ and 1.6 are consistent with the observations (Bouwens et al. 2007; McLure et al. 2013; Schenker et al. 2013; Finkelstein et al. 2014; Oesch et al. 2014; Bouwens et al. 2015b), while $m_{22} = 0.8$ has insufficient halos with $M_h \sim 10^{10} M_\odot$ at $z = 6 - 8$ (see text for details).

halos at various redshifts are sufficient to account for the observed counts, regardless of the underlying mass-luminosity ($M-L$) relation. However, the inferred mass-to-light ratio features a sharp, and probably unphysical, drop at the faint end (Bozek et al. 2015). This approach therefore provides a more conservative estimation of m_{22} . By contrast, the latter leads to a power-law $M-L$ relation at the faint end (Schultz et al. 2014), which is more plausible. However, it fundamentally assumes that CDM matches the observed LF perfectly and that ψ DM follows exactly the same $M-L$ relation as CDM, both of which may not be necessarily true. Consequently, any suppression in the ψ DM MF translates directly into a deficit of galaxies, resulting in a higher, and likely overestimated, lower limit for m_{22} .

Figure 5 shows our cumulative MFs for both CDM and ψ DM. CDM MF is constructed from a $30 h^{-1}$ Mpc simulation with 1024^3 particles, and ψ DM MF is obtained by integrating Equation (7). The 2σ uncertainties are estimated using bootstrap resampling over 125 subvolumes, each with a side length of $6 h^{-1}$ Mpc. Here the halo masses corresponding to various observational data points are determined by applying abundance matching to the CDM MF, which essentially forces observations to be consistent with CDM. In this approach, we find that the faintest galaxies currently observed at $z \sim 4 - 10$ all have $M_h \sim 10^{10} M_\odot$. We demonstrate that ψ DM with $m_{22} = 3.2$ and 1.6 are still consistent with the observations, while $m_{22} = 0.8$ does not have a sufficient number of halos with $M_h \sim 10^{10} M_\odot$ at $z = 6 - 8$. Using the recent LF of B15b leads to a lower limit of ψ DM particle mass, $m_{22} \geq 1.5$ (2σ). By contrast, to infer the results of applying abundance matching to the ψ DM MF, one can simply move the observational data points in Figure 5 to

TABLE 1
PARAMETERS OF THE CONDITIONAL LF MODEL

Model	L_0 (M_{AB})	M_1 (M_\odot)	Σ	p	q	r	χ_{red}^2
CDM	-20.7	2.7×10^{11}	0.16	1.6	1.2	1.9	1.4
$m_{22} = 3.2$	-20.9	3.1×10^{11}	0.16	1.5	1.2	1.9	1.5
$m_{22} = 1.6$	-21.1	4.0×10^{11}	0.16	1.4	1.2	1.9	1.9
$m_{22} = 0.8$	-21.7	7.8×10^{11}	0.16	1.2	1.1	1.8	3.1
B15b ^a	-21.9	1.2×10^{12}	0.16	1.2	1.0	1.5	

^a Bouwens et al. (2015b).

ward smaller halo masses until, if possible, touching the ψ DM cumulative MF with a specific particle mass. This approach decreases the lower limit to $m_{22} \geq 0.9$ (2σ), and hence significantly reduces the tension between observational constraints and smaller ψ DM particle masses.

We emphasize that the two estimations of ψ DM particle mass given above, namely, $m_{22} \geq 1.5$ and $m_{22} \geq 0.9$, are determined using two extreme models of M - L relation, and therefore likely bracket the uncertainty of the lower limit of m_{22} . In fact, for ψ DM, it does not make much sense to apply the M - L relation predicted by CDM from abundance matching. The lower limit $m_{22} \geq 1.5$ is therefore likely overestimated. In the next subsection we provide a more plausible estimation of m_{22} based on a less model-dependent M - L relation.

4.2. Luminosity Function

4.2.1. Conditional Luminosity Function

As our preferred method to constrain the ψ DM particle mass we adopt the conditional LF model (Cooray & Milosavljević 2005), which has been shown to be able to reproduce well the high- z UV LF in the context of CDM (Bouwens et al. 2008, 2015b). The conditional LF, denoted as $\phi_c(L|M_h, z)$, describes the probability density of halos with mass M_h hosting galaxies with UV luminosity of L . It is modeled by a lognormal distribution,

$$\phi_c(L|M_h, z) = \frac{1}{\sqrt{2\pi} \ln(10)\Sigma L} \exp\left\{-\frac{\log[L/L_c(M_h, z)]^2}{2\Sigma^2}\right\}, \quad (8)$$

which has a dispersion of $\ln(10)\Sigma$ and peaks at $L_c(M_h, z)$, the M - L relation of the central galaxy. Following B15b, we parameterize L_c as

$$L_c(M_h, z) = L_0 \frac{(M_h/M_1)^p}{1 + (M_h/M_1)^q} \left(\frac{1+z}{4.8}\right)^r, \quad (9)$$

where M_1 gives the characteristic halo mass. The M - L relation asymptotes to $L_c \propto M_h^p$ when $M_h \ll M_1$ and $L_c \propto M_h^{p-q}$ when $M_h \gg M_1$. For a given ϕ_c , the LF can then be calculated by

$$\phi(L, z) = \int_0^\infty \phi_c(L|M_h, z) \frac{dn}{dM_h}(M_h, z) dM_h, \quad (10)$$

where dn/dM_h is the halo MF.

Given the above conditional LF formalism, we then use chi-square fitting on the observed LF of B15b at $z = 5 - 10$ to determine the parameter set (L_0 , M_1 , Σ , p , q , r). Table 1 shows the best-fit parameters and the corresponding reduced chi-square (χ_{red}^2). We fix Σ to 0.16 both because it is not well constrained owing to the

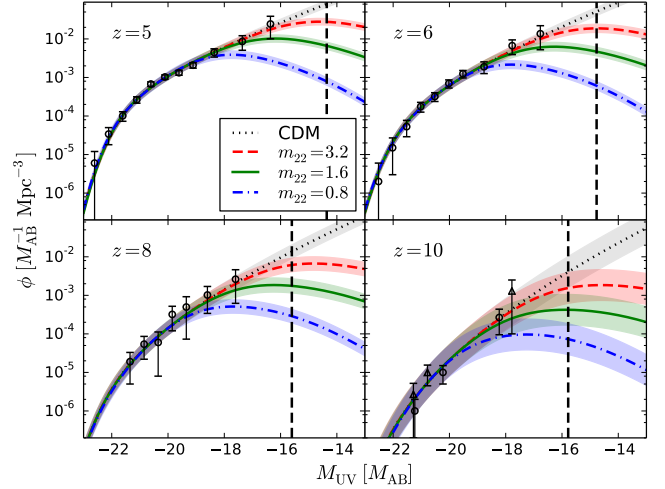


FIG. 6.— Luminosity function (LF) at $z = 5 - 10$ predicted by the conditional LF model. The shaded regions indicate the 2σ uncertainties. Error bars show the observed LFs (2σ at $z = 5 - 8$ and 1σ at $z = 10$) of B15b (open circles) and Oesch et al. (2014, open triangles). ψ DM LF shows a drop at the faint end due to the suppression of low-mass halos. $m_{22} = 3.2$ and 1.6 are consistent with the observations, while $m_{22} = 0.8$ shows a deficit of faint galaxies with $M_{UV} \gtrsim -18$, especially at $z \leq 6$ (see text for details). Vertical dashed lines highlight the limiting absolute magnitudes of JWST, which are assumed to be two magnitudes fainter than those of HST.

substantial uncertainties at the bright end and because it does not influence the faint-end slope, which is most important for constraining m_{22} . Note that the faint-end M - L relation, $L_c \propto M_h^p$, is flatter for smaller m_{22} so as to compensate for the stronger suppression of faint galaxies. In addition, note that from Equation (9) the faintest galaxies currently observed at $z \sim 4 - 10$ all have $M_h \sim 10^{10} M_\odot$, consistent with the results obtained by applying abundance matching to CDM (see Fig. 5). A limiting absolute magnitude of $M_{UV} \sim -15$ at $z \sim 6$, appropriate for JWST, corresponds to $M_h \sim 4 \times 10^9 M_\odot$.

Figure 6 shows our predicted galaxy UV LF at $z = 5 - 10$ using the conditional LF formalism described above. We use the ST99 MF for CDM, and combine it with the ratio given in Equation (7) to get the ψ DM MFs with various m_{22} . We add 2σ variations estimated from the MF at $M_h \sim 10^{10} M_\odot$ in our $30 h^{-1}$ Mpc simulations to capture the uncertainties of the predicted LF around the faintest LF bins of B15b. The ψ DM LF shows a clear decline at the faint end, which is distinctly different from the CDM prediction and will be directly testable with forthcoming observations such as JWST. Note that this feature results from the assumption of a power-law M - L relation at the faint end (Eq. [9]), and thus cannot be captured by the usual abundance matching. The cases $m_{22} = 3.2$ and 1.6 are found to be consistent with the current observations, while $m_{22} = 0.8$ shows an apparent deficit of faint galaxies with $M_{UV} \gtrsim -18$, especially at $z \leq 6$. This result is consistent with the analysis of cumulative MF (see Figure 5). Using the faintest LF bins of B15b (open circles in Fig. 6) leads to $m_{22} \geq 1.2$ (2σ). Note that this constraint lies in-between those obtained in Section 4.1 ($m_{22} \geq 0.9$ and 1.5), as expected, since the faint-end M - L relation adopted here can be regarded as a compromise between the two extreme cases using abundance matching to CDM and to ψ DM MFs,

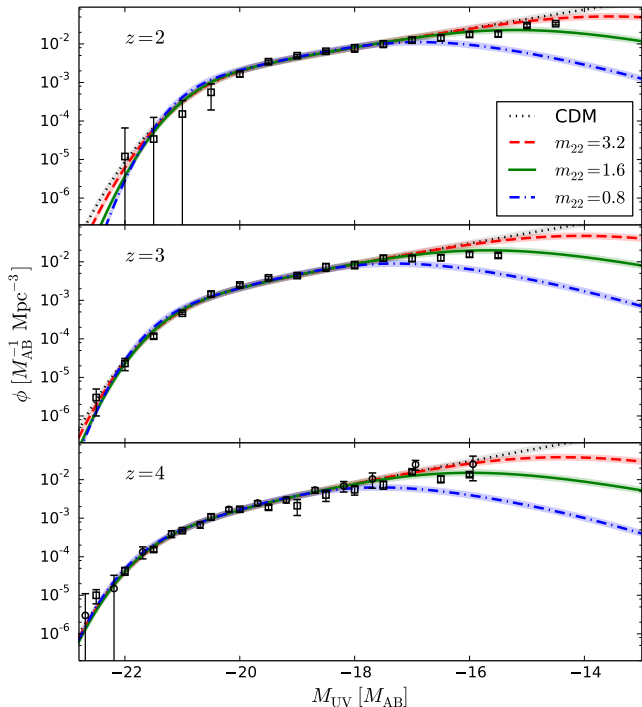


FIG. 7.— Luminosity function (LF) at $z = 2 - 4$ predicted by the conditional LF model. The shaded regions indicate the 2σ uncertainties. The data with 2σ error bars are the LFs determined from B15b (open circles) and Parsa et al. (2015, open squares). The observed faint-end slope in this redshift range is consistent with the ψ DM model with $m_{22} \sim 1.6$ (see text). Notice that CDM overestimates the number density of faint galaxies, especially at $z = 3$.

respectively.

It is also interesting to extend the comparison of LF to $z < 5$ (Fig. 7). To be self-consistent, we adopt the same parameters of the conditional LF model shown in Table 1. Parsa et al. (2015) recently found a much shallower faint-end slope at $z = 2 - 4$, distinctly different from the steep slope reported previously (Reddy & Steidel 2009; Alavi et al. 2014; Bouwens et al. 2015b). ψ DM with $m_{22} \sim 1.6$ is found to provide a clear better fit to this shallower slope, while CDM overestimates the number density of faint galaxies, especially at $z = 3$. It is thus very important for future research to understand this apparent discrepancy between the faint-end slopes determined by Parsa et al. (2015) and the previous studies at $z < 5$.

It should be emphasized that the conditional LF model provides a more reasonable constraint on the ψ DM particle mass. At first glance, it may seem that this approach has too many free parameters to provide an appropriate estimation. However, actually the only relevant parameter for constraining m_{22} is p , the faint-end slope of the $M-L$ relation, as argued below. Since the faint-end slope of the LF is insensitive to Σ , we have $L \sim L_c \propto M_h^p$. This leads to $\phi(M_{UV}) = 0.4 \ln(10) L \phi(L) = 0.4 \ln(10) p^{-1} dn/d\ln M_h$, where $dn/d\ln M_h$ is the halo MF in logarithmic mass bins. Therefore, for a given p , a maximum observed $\phi(M_{UV})$ can be directly converted to a minimum required peak $dn/d\ln M_h$, which then turns into a lower limit of m_{22} . Moreover, if $dn/d\ln M_h \propto M_h^\eta$, which is appropriate when $M_h \gg M_0$ in Equation (7)

(i.e., when ψ DM is still close to CDM), then $\phi(L) \propto L^{\eta/p-1}$. Since η can be estimated by the ST99 MF, we can determine p from a given $\phi(L)$. Accordingly, p itself is not unconstrained.

As an example, consider the ψ DM model with $m_{22} = 1.6$ at $z = 6$. The observed LF has $\phi(L) \propto L^{-2.1}$ at $M_{UV} \sim -19$. This luminosity corresponds to a halo mass of $M_h \sim 7 \times 10^{10} M_\odot$, at which $dn/d\ln M_h \propto M_h^{-1.5}$ (see Fig. 4). We thus have $p = -1.5/(-2.1 + 1) \sim 1.4$, consistent with Table 1. The MF has a peak of $dn/d\ln M_h \sim (1.0 \pm 0.3) \times 10^{-2} \text{ Mpc}^{-3}$ around $M_h = 10^{10} M_\odot$, which can then be converted to a maximum LF of $\phi(M_{UV}) = (6.8 \pm 2.0) \times 10^{-3} \text{ Mpc}^{-3}$. This estimation is in excellent agreement with Figure 6, even though the only assumption made here is that the $M-L$ relation is a power law at the faint end. Therefore, we conclude that the conditional LF model provides a more plausible and less model-dependent estimation of the ψ DM particle mass than with abundance matching.

4.2.2. Truncated Schechter Function

It is also useful and convenient to parameterize the predicted LF of ψ DM by a formula similar to the Schechter function. We adopt

$$\phi(L) = \frac{\phi_\star}{L_\star} \left(\frac{L}{L_\star} \right)^\alpha \exp\left(-\frac{L}{L_\star}\right) \Gamma(L), \quad (11)$$

where

$$\Gamma(L) = \left[1 + \left(\frac{L}{L_\psi} \right)^\gamma \right]^{\beta/\gamma} \quad (12)$$

represents the suppression of faint galaxies in ψ DM ($\Gamma = 1$ for CDM). L_ψ is the characteristic luminosity of the suppression, below which $\phi(L)$ asymptotes to $L^{\alpha+\beta}$. To describe the time evolution of LF, we follow the literature (Bouwens et al. 2012; Kuhlen & Faucher-Giguère 2012; Schultz et al. 2014; Bouwens et al. 2015a) and assume that the parameters in Equations (11) and (12) depend linearly on redshift. Applying chi-square fitting to the conditional LF model (Fig. 6) then leads to

$$\begin{aligned} M_{UV,\star} &= -20.90 - 0.004(z - 6) \\ \phi_\star &= 0.52 \times 10^{-0.28(z-6)-3} \text{ Mpc}^{-3} \\ \alpha &= -1.78 - 0.06(z - 6) \\ M_{UV,\psi} &= -17.44 + 5.19 \log(m_{22}/0.8) - 2.71 \log((1+z)/7) \\ \beta &= 1.69 + 0.03(z - 6) \\ \gamma &= -1.10, \end{aligned} \quad (13)$$

where we have assumed $M_{UV} = -2.5 \log(L/\text{erg s}^{-1} \text{ Hz}^{-1}) + 51.6$.

Figure 8 shows the LF obtained by the truncated Schechter function described above. It fits well with the LF predicted by the conditional LF model at $z = 4 - 8$, while for the bright end at $z = 10$ it slightly outnumbers the observed galaxies (see B15b and references therein) and is marginally consistent with the conditional LF model. This subtle discrepancy mainly results from the assumption of linear dependence on redshift in Equation (13), and it is unclear whether it indicates a faster evolution at $z > 8$ given the substantial uncertainties in the LF at $z = 10$. This possible acceleration in evolution

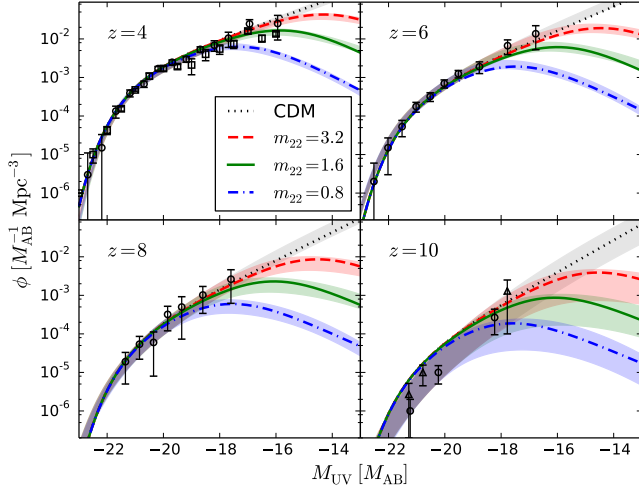


FIG. 8.— Luminosity function (LF) at $z = 4 - 10$ obtained by a single analytic formula similar to the Schechter function (Eqs. [11-13]; central lines). The shaded regions are the same as Fig. 6, showing the LF predicted by the conditional LF model within 2σ . Error bars show the observed LFs (2σ at $z = 4-8$ and 1σ at $z = 10$) of Parsa et al. (2015, open squares), B15b (open circles), and Oesch et al. (2014, open triangles). The analytic formula well reproduces the conditional LF results at $z = 4 - 8$, while at $z = 10$ it slightly outnumbers the observed galaxies and is marginally consistent with the conditional LF model.

has been successfully modeled recently in the context of abundance matching for CDM by additionally incorporating early stellar evolution (Mason et al. 2015). It may be interesting to apply this approach in the context of ψ DM too for extending predictions to $z \geq 10$ with some security.

4.3. Magnification Bias for the Hubble Frontier Fields

We have seen above that the quantum pressure inherent to ψ DM leads to a suppression of low-mass galaxies and hence our predictions for the LF have largest contrast with CDM at low luminosities. Here we examine the benefits of gravitational magnification in the new HFF data, where statistical samples of multiply lensed galaxies are magnified by typically ~ 10 (Lam et al. 2014), reaching two magnitudes or more further down the LF at high redshifts. It corresponds to an intrinsic UV luminosity of $M_{UV} \sim -15$, where we predict sizeable difference between CDM and ψ DM for the interesting range of m_{22} needed to provide the kpc-scale dark cores of local dSph galaxies.

Gravitational lensing induces a bias in the number density of sources detected above a flux limit, which in the case of lensing clusters is well established (Broadhurst et al. 1995; Umetsu & Broadhurst 2008) and has led to the detection of the highest redshift and lowest luminosity galaxies currently known (Zheng et al. 2012; Coe et al. 2013; Zitrin et al. 2014). The number density of such high-redshift galaxies is modified in the following way:

$$N_{\text{lensed}}(>L) = (1/\mu)N_{\text{unlensed}}(>L/\mu), \quad (14)$$

where μ is the magnification factor and $N(>L)$ is the galaxy number density above a flux limit corresponding to L . It shows the competition between the enhanced number density due to the lower, magnified limiting luminosity and the diminished source plane area, which is

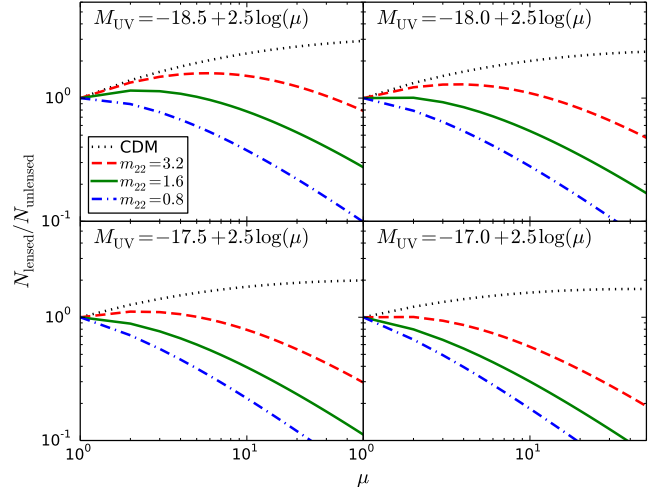


FIG. 9.— Magnification bias predicted by ψ DM and CDM at $z = 10$. The numbers on the top of each panel indicate the adopted limiting luminosities. For CDM the magnification bias continually rises owing to the steep faint-end slope of the LF, whereas for ψ DM the bias is generally lower than one because of the strong suppression of low-mass halos. The lower the limiting luminosity, the greater the contrast between ψ DM and CDM.

smaller than the observed area by the same magnification factor. The magnification bias can thus be defined as $N_{\text{lensed}}(>L)/N_{\text{unlensed}}(>L)$, which equals one when there is no bias.

Figure 9 shows the difference between the magnification bias for CDM and ψ DM at $z = 10$, which we predict to be a strong function of limiting luminosity because of the difference in sign in the faint-end slope of the LFs between these two models. CDM is continually rising and hence the magnification bias is greater than one, thereby enhancing the number of faint galaxies detected at high redshifts, whereas for ψ DM the turnover in the LF leads to many fewer galaxies magnified above the flux limit. The difference we predict at $M_{UV} = -14.5$ for example is a factor of ~ 10 for $\mu \sim 10$ at $z \sim 10$ between CDM and ψ DM with $m_{22} \sim 1.2$. Going beyond this with JWST should probe another two magnitudes deeper with the assistance of lensing (Mason et al. 2015) - most efficiently by employing the same deep lenses as the HFF for which the magnification maps have been widely studied (Rodney et al. 2015) and best understood (Lam et al. 2014; Diego et al. 2015).

4.4. Reionization

Based on the predicted ψ DM LF, we can calculate the reionization history using the standard approach that has been adopted for various dark matter models (e.g., Kuhlen & Faucher-Giguère 2012; Schultz et al. 2014; Bozek et al. 2015). The time evolution of the volume filling fraction of ionized hydrogen, $Q_{\text{HII}}(z)$, is governed by

$$\frac{dQ_{\text{HII}}}{dt} = \frac{\dot{n}_{\text{ion}}}{\bar{n}_{\text{H}}} - \frac{Q_{\text{HII}}}{\bar{t}_{\text{rec}}}, \quad (15)$$

where \bar{n}_{H} is the mean comoving hydrogen number density. We take $Q_{\text{HII}} = 0$ at $z = 25$. The volume-averaged recombination time, $\bar{t}_{\text{rec}}(z)$, can be determined by

$$\bar{t}_{\text{rec}} \sim 0.93 \left(\frac{C_{\text{HII}}}{3} \right)^{-1} \left(\frac{1+z}{7} \right)^{-3} \text{ Gyr}, \quad (16)$$

where $C_{\text{HII}} \equiv \langle n_{\text{HII}}^2 \rangle / \langle n_{\text{HII}} \rangle^2$ is the volume-averaged clumping factor. Here we have assumed an intergalactic medium temperature of 2×10^4 K and a primordial hydrogen mass fraction of 0.76.

The comoving ionizing emissivity, $\dot{n}_{\text{ion}}(z)$, defined as the number of ionizing photons produced per unit time per unit comoving volume, can be estimated from the galaxy UV LF:

$$\dot{n}_{\text{ion}} = \frac{2 \times 10^{25}}{\text{erg Hz}^{-1}} \zeta_{\text{ion}} f_{\text{esc}} \int_{L_{\text{lim}}}^{\infty} dL \phi(L) L, \quad (17)$$

where ζ_{ion} represents the efficiency of converting galaxy UV luminosity to ionizing photon luminosity, and f_{esc} is the escape fraction. Strictly speaking, since the observed rest-frame UV luminosity (at ~ 1500 Å) will also be extinguished by dust, f_{esc} in Equation (17) is the *relative* escape fraction (Steidel et al. 2001) defined as the *absolute* escape fraction (the fraction of ‘ionizing photons’ that escapes the galaxy without being absorbed by dust and neutral hydrogen) divided by the fraction of ‘UV photons’ that escapes. This relative escape fraction can be significantly higher than the absolute escape fraction because of the efficient dust extinction at ~ 1500 Å. $M_{\text{lim}} = -2.5 \log(L_{\text{lim}}/\text{erg s}^{-1} \text{Hz}^{-1}) + 51.6$ is the limiting UV magnitude, below which the galaxy formation is assumed to be inefficient. Note that \dot{n}_{ion} is sensitive to the faint-end slope of LF that differentiates various dark matter models.

For a given $Q_{\text{HII}}(z)$, the Thomson optical depth to CMB can be calculated via

$$\tau_e = c \sigma_T \bar{n}_H \int_0^{\infty} dz \frac{(1+z)^2}{H(z)} Q_{\text{HII}}(z) (1 + \eta(z) Y/4X), \quad (18)$$

where σ_T is the Thomson cross-section, $H(z)$ is the Hubble parameter, $X \sim 0.76$ and $Y = 1 - X$ are the primordial mass fraction of hydrogen and helium, respectively, and we take $\eta(z > 4) = 1$ when helium is only singly ionized and $\eta(z \leq 4) = 2$ when helium is doubly ionized by quasars.

There are three free parameters in Equations (15)-(18), namely, C_{HII} , M_{lim} , $\zeta_{\text{ion}} f_{\text{esc}}$ (ζ_{ion} and f_{esc} are fully degenerate), which, for simplicity, are assumed to be spatially uniform and redshift-independent in this work. The typical parameter ranges adopted in the literature are $C_{\text{HII}} = 2 \sim 5$, $M_{\text{lim}} = -17 \sim -10$, $\zeta_{\text{ion}} = 0.5 \sim 2.0$, and $f_{\text{esc}} = 0.1 \sim 0.5$ (Bouwens et al. 2012; Kuhlen & Faucher-Giguère 2012; Schultz et al. 2014; Bozek et al. 2015; Bouwens et al. 2015a; Robertson et al. 2015). To bracket the uncertainties in these parameters, we consider three different parameter sets: a minimum reionization model (MIN) with $(C_{\text{HII}}, \zeta_{\text{ion}} f_{\text{esc}}, M_{\text{lim}}) = (4.0, 0.2, -13)$, a fiducial reionization model (FID) with $(C_{\text{HII}}, \zeta_{\text{ion}} f_{\text{esc}}, M_{\text{lim}}) = (3.0, 0.6, -13)$, and a maximum reionization model (MAX) with $(C_{\text{HII}}, \zeta_{\text{ion}} f_{\text{esc}}, M_{\text{lim}}) = (2.0, 1.0, -13)$. The adopted values are also shown in Table 2. Note that since ψDM should be insensitive to M_{lim} (because of the strong suppression of small halos), we fix $M_{\text{lim}} = -13$ unless otherwise specified.

Figure 10 shows the time evolution of Q_{HII} for various models. For a given reionization parameters, ψDM predicts a faster increase of ionized volume at later times. Recent observations indicate that reionization undergoes

TABLE 2
REIONIZATION PARAMETERS

Model	C_{HII}	$\zeta_{\text{ion}} f_{\text{esc}}$	M_{lim}^a
MIN	4.0	0.2	-13
FID	3.0	0.6	-13
MAX	2.0	1.0	-13

^a M_{lim} is allowed to vary when computing τ_e .

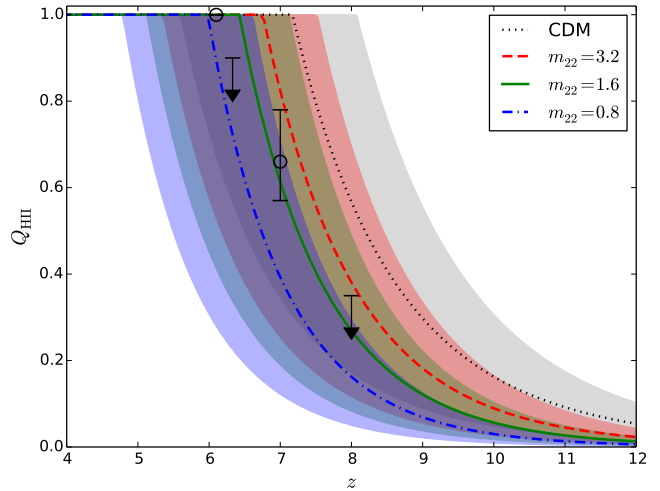


FIG. 10.— Volume filling fraction of HII as a function of redshift. The central lines correspond to the MIN model and the shaded regions are bounded by the MIN and MAX models. The limiting UV magnitude is fixed to $M_{\text{lim}} = -13$. Open circles and arrows mark the observational constraints at $z \sim 6 - 8$ (Fan et al. 2006; Schroeder et al. 2013; Schenker et al. 2014; McGreer et al. 2015).

a rapid evolution at $6 < z < 8$ and is completed at $z \sim 6$ (Fan et al. 2006; Schroeder et al. 2013; Schenker et al. 2014; McGreer et al. 2015). Correspondingly, the required ionizing photon production efficiency, $\zeta_{\text{ion}} f_{\text{esc}}$, is ~ 0.6 for ψDM with $m_{22} = 0.8$, about two times higher than CDM ($\zeta_{\text{ion}} f_{\text{esc}} \sim 0.3$). For ψDM this result is insensitive to the values of both M_{lim} and C_{HII} probed in this work.

Figure 11 shows the Thomson optical depth as a function of M_{lim} for various models. Most recent Planck 2015 results give $\tau_e = 0.066 \pm 0.016$ (1σ , Planck Collaboration et al. 2015), which is marginally consistent with $m_{22} = 0.8$ assuming $\zeta_{\text{ion}} f_{\text{esc}} \sim 0.6$, in agreement with the estimation from $Q_{\text{HII}}(z)$. Note that this estimation is largely independent of both C_{HII} and M_{lim} when $M_{\text{lim}} \gtrsim -15$, since galaxies fainter than this magnitude are highly suppressed at $z \geq 6$ even for $m_{22} = 3.2$. Given the considerable uncertainties in the reionization model at high redshifts, it is therefore clear that neither $Q_{\text{HII}}(z)$ nor τ_e provides a stringent constraint on ψDM even for $m_{22} \sim 0.8$. In comparison, CDM with an ionizing photon production efficiency as low as $\zeta_{\text{ion}} f_{\text{esc}} \sim 0.2$ can be consistent with Planck 2015 assuming $M_{\text{lim}} \gtrsim -13$, in agreement with the findings of Bouwens et al. (2015a) and Robertson et al. (2015).

Bozek et al. (2015) used a similar approach to estimate the ψDM particle mass. They reported that $m_{22} = 1.0$ is disfavored by the observed value of τ_e at 3σ , and consequently a particle mass as high as $m_{22} = 10$ is required, significantly higher than our estimation. This

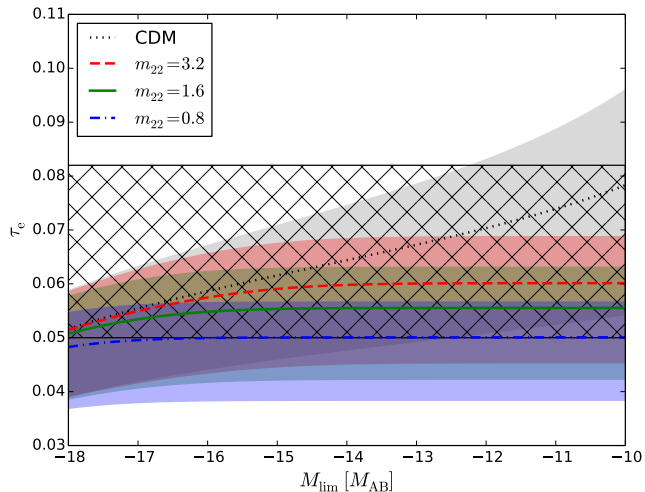


FIG. 11.— Thomson optical depth versus limiting UV magnitude. The central lines correspond to the FID model and the shaded regions are bounded by the MIN and MAX models, where M_{lim} is allowed to vary. The cross-hatched region shows the Planck 2015 1σ confidence limit (Planck Collaboration et al. 2015).

inconsistency with our result mainly arises from a higher value of τ_e they adopted from the previous Planck 2013 results, $\tau_e = 0.090 \pm 0.013$ (1σ , Planck Collaboration et al. 2014; Spergel et al. 2015). Also note that the LF we predict based on the ‘conditional LF model’ declines at the faint end (see Fig. 6), while the LF adopted by Bozek et al. (2015) based on the ‘abundance matching’ approach does not have this natural feature. Such relative deficit of faint galaxies in our LF model would only delay the reionization process and reduce the Thomson optical depth, hence increasing the discrepancy between observations and the ψ DM model with a small particle mass. However, here we demonstrate that $m_{22} \sim 0.8$ can still be consistent with the latest Planck observations provided that the ionizing photon production efficiency is sufficiently high.

5. DISCUSSION AND CONCLUSION

In this paper, we have constructed cosmological simulations designed to study the dark matter halo MF in the wave dark matter (ψ DM) scenario. Here the uncertainty principle counters gravity below a Jeans scale, which is determined by the only free parameter in this model, m_{22} , the dark matter particle mass. The smaller the particle mass, the larger the Jeans scale, and hence the stronger the suppression of low-mass halos. For this reason, we focus on determining a lower limit of m_{22} based on the observed UV LF at $z \sim 4-10$ and the reionization history.

The major findings in this study can be briefly summarized as follows:

- ψ DM halo MF has a prominent drop below $\sim 10^{10} M_{\odot}$, which can be well fitted by Equation (7).
- ψ DM predicts a clear drop in the galaxy LF around $M_{\text{UV}} \gtrsim -16$ at $z \gtrsim 4$ based on a conditional LF model, which can be fitted by a truncated Schechter function (Eqs. [11-13]).
- The newly established LF at $z \sim 4-10$ constrains the ψ DM particle mass to be $m_{22} \geq 1.2$ (2σ).

- For galaxies magnified $>10\times$ in the Hubble Frontier Fields, ψ DM predicts an order of magnitude fewer detections than CDM at $z \gtrsim 10$ down to an intrinsic UV luminosity of $M_{\text{UV}} \sim -15$.
- ψ DM with $m_{22} \gtrsim 0.74$ can satisfy the Thomson optical depth reported by the latest Planck observations, on the assumption of a reasonable ionizing photon production rate.

In the following we give a more thorough discussion of this work. We first argue that, for studying the ψ DM MF with the particle masses, redshift range, and halo masses of interest here ($m_{22} \sim 1$, $z \sim 4-10$, $M_{\text{h}} \gtrsim 1 \times 10^9 M_{\odot}$), it is reasonable to approximate both the ψ DM transfer function as redshift-independent and the evolution of quantum fluid by collisionless particles. The major drawback of these approximations is the inability to capture the difference in the substructures between CDM and ψ DM halos, where ψ DM halos have prominent solitonic cores in the centers surrounded by fine-scale, large-amplitude cellular interference (SCB14a, S14b). However, this shortcoming is irrelevant when one is only concerned with the halo masses, as in this work. This is especially true because most halos above $\sim 10^9 M_{\odot}$ have yet to merge gravitationally with each other at $z \gtrsim 4$.

Simulations of collisionless particles with a cut-off in the initial power spectrum suffer from the well-known side effect of inducing spurious halos due to numerical artefacts, which must be accounted for when determining an accurate MF at low masses. To identify and remove these artificial halos, we adopt a similar approach suggested by Lovell et al. (2014) based on the shape of the progenitors of halos and the spatial overlap between low-resolution halos and their high-resolution counterparts (see Appendix A). The resulting MF cleaned in this way then shows a clear decline as expected below the Jeans mass and can be well fitted by Equation (7). Most importantly, this reinforces the MF we derive above $\gtrsim 3 \times 10^9 M_{\odot}$, which are most relevant for comparing with observations.

Comparing the halo MF with the observed UV LF requires the knowledge of $M-L$ relation. For this purpose, we first apply the abundance matching technique to either CDM or ψ DM MFs. In both cases, ψ DM with $m_{22} = 0.8$ shows a deficit of low-mass galaxies with $M_{\text{h}} \sim 10^{10} M_{\odot}$ at $z = 6-8$ (see Fig. 5), leading to lower limits of particle mass, $m_{22} \geq 1.5$ (abundance matching to CDM) and $m_{22} \geq 0.9$ (abundance matching to ψ DM). We also explore the conditional LF model as an alternative approach, which yields $m_{22} \geq 1.2$. The key assumption here is a power-law $M-L$ relation at the faint end. We argue that this approach provides a more reasonable and model-independent estimation of the ψ DM particle mass. In addition, we predict that the high- z LF should turn over slowly around $M_{\text{UV}} \gtrsim -16$ at $z \gtrsim 4$, distinctly different from CDM. This predicted feature lies just beyond the detected luminosity range of the current LFs at $z \gtrsim 4$, but will be directly testable with forthcoming observations such as JWST and also with highly magnified galaxies in the HFF data.

Note that the $M-L$ relation for low-mass halos may be subject to large uncertainties. Strigari et al. (2008) showed that the Milky Way dwarf satellites, which have

$M_h \lesssim 10^{10} M_\odot$, share a common mass scale but have luminosity differences over four orders of magnitude. Therefore, a more complicated M - L relation might be expected for halos below $\sim 10^{10} M_\odot$, at least at lower redshifts. Even in CDM simulations, O’Shea et al. (2015) found a relatively flat high- z LF at the faint end compared with the Schechter function fits to observations (B15b). Ideally, ψ DM simulations with the addition of baryonic physics may be very helpful in further differentiating the high- z LFs predicted by CDM and ψ DM.

The Thomson scattering optical depth to CMB provides another constraint for the ψ DM particles mass. In general, ψ DM predicts a faster increase of ionized volume at later times due to the suppression of early galaxy formation. We demonstrate that ψ DM with $m_{22} \gtrsim 0.74$ can satisfy the Planck 2015 results and have reionization completed at $z \gtrsim 6$, on the assumption that the ionizing photon production rate is sufficiently efficient (about three times higher than that required for CDM). This result is largely independent of the limiting luminosity and the faint-end slope adopted since galaxies fainter than $M_{UV} \sim -15$ are highly suppressed at $z \geq 6$ even for $m_{22} = 3.2$. On the other hand, this constraint is somewhat undermined because of the current large uncertainties associated with the escape fraction and the efficiency of converting galaxy UV luminosity to ionizing photon luminosity. Note that for CDM the reionization calculation is much more uncertain in fact than for ψ DM, as it is dominated by the choice of limiting luminosity assumed for the relatively steeply rising LF ($\alpha > 1.0$) as otherwise the integrated luminosity diverges.

The MF below $\sim 10^9 M_\odot$ determined by our simulations has a larger relative uncertainty in our model. Firstly, approximating the ψ DM transfer function as redshift-independent can somewhat underestimate the matter power spectra at higher redshifts (see Fig. 1), which in turn leads to an underestimation of MF at low masses. Secondly, we approximate the evolution of quantum fluid by collisionless particles. It may allow for the formation of a small number of halos with masses well below the Jeans mass, which would otherwise be suppressed further if the dynamical effect of quantum pressure is taken into account. In this sense, the MF in a bona-fide wave-based ψ DM simulation may have an even stronger break at the low-mass end than Figure 4. We may hope to check on this in the future by running the full adaptive-mesh-refinement wave simulations that we have previously described (SCB14a, S14b) on a substantially more powerful platform. Thirdly, there are also uncertainties associated with the removal of spurious halos below $\sim 10^9 M_\odot$ (see the shaded areas in Fig. 4). However, it should be emphasized that none of these uncertainties are relevant for the purpose of this study at the level of precision that is currently afforded by the data, as the depths of the current Hubble and forthcoming JWST do not extend to such low-mass halos.

Though not entirely consistent, the ψ DM particle mass estimated in this work, $m_{22} \geq 1.2$ (2σ), is surprisingly close to the values determined from local dwarf galaxies. SCB14a established with the first wave-based ψ DM simulations a distinct solitonic core in the center of every ψ DM halo. We have previously obtained $m_{22} = 0.8 \pm 0.2$ (1σ) by fitting the spatial distribution of the intermediate metallicity stellar population in the Fornax dSph

galaxy to the soliton mass profile, under the assumption of a constant projected velocity dispersion. Marsh & Pop (2015) have also determined a similar constraint, $m_{22} \leq 1.1$ (2σ), by fitting the mass profiles of Fornax and Sculptor dSph galaxies to the soliton mass profile using an empirical relation between the half-light radius and velocity dispersion. Note that for $m_{22} = 1.2$, we predict that a halo with $M_h = 2 \times 10^9 M_\odot$ still has a core as large as ~ 1.1 kpc (S14b), consistent with many estimates of the large cores found in dSph galaxies (e.g., Salucci et al. 2012; Amorisco et al. 2013). A more thorough comparison between the stellar phase-space distribution in dSph galaxies and the ψ DM halo mass profile using a full Jeans analysis will be extremely important to further clarify how coincident are the particle masses determined by these various approaches and the role of baryonic feedback in this context (S-R. Chen et al., in preparation). The inherent density granularity of the ψ DM halo may also be examined through internal dynamical effects and by lensing flux anomalies on sub-kpc scales, which provide other key independent observational tests for distinguishing ψ DM from WDM and CDM.

The finding that a similar particle mass in ψ DM can both solve the cusp-core problem in dwarf galaxies (Moore 1994) and satisfy the high- z LF and reionization observations is very encouraging for this model. It demonstrates a great advantage of ψ DM over WDM, for which the light particle mass required for creating kpc-scale cores in dSph galaxies prevents the formation of the host dwarf galaxies in the first place and overly suppresses high- z galaxies (Macciò et al. 2012; Schneider et al. 2014). The key reason for this striking difference is that the relation between core radius and power spectrum truncation differs because of the very different physics underlying ψ DM and WDM, with the uncertainty principle responsible in the case of ψ DM and free streaming in the case of WDM. The particle masses in the two models can always be chosen so that they have similar truncated matter power spectra, but the corresponding core radius in ψ DM can then be several times larger than that in WDM. This is why ψ DM *does not suffer from the Catch 22 problem affecting WDM*.

6. ACKNOWLEDGEMENT

We thank David Marsh for stimulating discussions. This work is supported in part by the National Science Council of Taiwan under the grant MOST 103-2112-M-002-020-MY3.

APPENDIX

A. REMOVAL OF SPURIOUS HALOS

Particle simulations with an initial power spectrum cut-off suffer from the formation of spurious halos, especially at low masses. It is therefore necessary to adopt a robust algorithm to identify genuine halos in the simulations, which we describe below.

We first use the AMIGA Halo Finder (AHF, Knollmann & Knebe 2009) to identify all halos (both genuine and spurious halos), and find the corresponding protohalos by tracing the constituting particles back to the initial redshift. We then define the protohalo sphericity as

$$S = \sqrt{\frac{I_1 + I_2 - I_3}{-I_1 + I_2 + I_3}}, \quad (\text{A1})$$

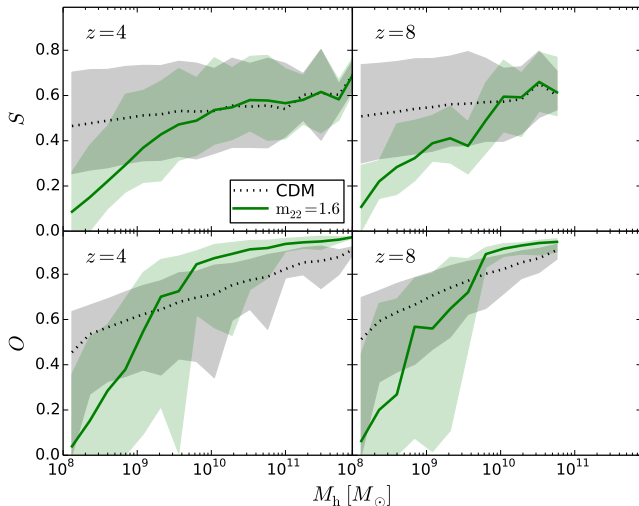


FIG. A1.— Sphericity and spatial overlap factor as a function of halo mass in the $15 h^{-1}$ Mpc simulations. The central solid and dotted lines show the mean values, and the shaded areas contain 95% of halos. Low-mass ψ DM halos have lower sphericity and overlap factor compared with CDM halos, especially for $M_h \lesssim 10^9 M_\odot$, indicative of a severe contamination from spurious halos in this mass range.

where $I_1 \leq I_2 \leq I_3$ are the principle moments of inertia of a protohalo. This is equivalent to having $S = c/a$, where a and c are the maximum and minimum semi-axis lengths of an ellipsoid of uniform density with the same principle moments of inertia as the protohalo (Lovell et al. 2014). Figure A1 (upper panel) shows the sphericity as a function of halo mass for both CDM and ψ DM with $m_{22} = 1.6$ in the $15 h^{-1}$ Mpc simulations with 512³ particles. Clearly, CDM halos have higher S . The average S of ψ DM halos lies below the 2σ lower limit of CDM halos for $M_h \lesssim 10^9 M_\odot$, indicative of a severe contamination from spurious ψ DM halos in this mass range.

To quantify the matching accuracy between two protohalos in low- and high-resolution simulations, respectively, we introduce a spatial overlap factor,

$$O = \frac{V_{\text{low}} \cap V_{\text{high}}}{V_{\text{low}} \cup V_{\text{high}}}, \quad (\text{A2})$$

where V is the volume of a protohalo estimated by depositing particles onto grids using the cloud-in-cell scheme with a cloud size equal to the mean particle separation. $V_{\text{low}} \cap V_{\text{high}}$ and $V_{\text{low}} \cup V_{\text{high}}$ represent the intersection and union of two volumes, respectively. Accordingly, $O = 1$ if the spatial distribution of two protohalos are completely overlapped, while $O = 0$ if there is no overlap at all. Note that our definition of spatial overlap factor differs from that of Lovell et al. (2014, see Eq. 6 therein). Equation (A2) does not require solving the gravitational potential and thus is more computationally efficient and more sensitive to the actual spatial overlap between two protohalos. Figure A1 (lower panel) shows the spatial overlap factor as a function of halo mass. The average O of ψ DM halos shows an apparent drop at $M_h \lesssim 10^9 M_\odot$, again suggesting that spurious halos start to outnumber genuine halos.

We consider most CDM halos as genuine since its MF is consistent with the analytic prediction of ST99 above $\sim 3 \times 10^8 M_\odot$ (corresponding to ~ 100 particles in our lower resolution simulations). We thus define the 2σ lower limit of S and O at $M_h = 3 \times 10^8 M_\odot$ in CDM as the minimum thresholds, S_{cut} and O_{cut} , below which halos are regarded as spurious. S_{cut} and O_{cut} slightly increase with redshift, and we take $S_{\text{cut}} = 0.31$ and $O_{\text{cut}} = 0.34$ by averaging over $z = 4 - 10$. Note that we do not use the mass cut criterion adopted by Lovell et al. (2014), which relies on extrapolating the low-resolution results to high-resolution runs.

In short, for each low-resolution halo identified by AHF, we calculate S by Equation (A1) and determine the highest value of O by applying Equation (A2) for all nearby high-resolution halos. Then, we use CDM halos to determine the minimum thresholds, S_{cut} and O_{cut} , and only low-resolution halos with $S \geq S_{\text{cut}}$ and $O \geq O_{\text{cut}}$ are marked as genuine. Figure 3 (lower panel) shows the spatial distribution of genuine halos. Clearly, suspicious low-mass halos, most visible along filaments, are removed with the above procedure, while only massive halos with a good match between low- and high-resolution simulations are retained.

REFERENCES

- Akerib, D. S., et al. 2014, *Phys. Rev. Lett.*, 112, 091303
Alavi, A., Siana, B., Richard, J., et al. 2014, *ApJ*, 780, 143
Amendola, L., & Barbieri, R. 2006, *Physics Letters B*, 642, 192
Amorisco, N. C., Agnello, A., & Evans, N. W. 2013, *MNRAS*, 429, L89
Angulo, R. E., Hahn, O., & Abel, T. 2013, *MNRAS*, 434, 3337
Arvanitaki, A., Dimopoulos, S., Dubovsky, S., Kaloper, N., & March-Russell, J. 2010, *Phys. Rev. D*, 81, 123530
Arvanitaki, A., & Dubovsky, S. 2011, *Phys. Rev. D*, 83, 044026
Becker, G. D., Bolton, J. S., Madau, P., et al. 2015, *MNRAS*, 447, 3402
Böhmer, C. G., & Harko, T. 2007, *J. Cosmology Astropart. Phys.*, 6, 25
Booth, C. M., Schaye, J., Delgado, J. D., & Dalla Vecchia, C. 2012, *MNRAS*, 420, 1053
Bouwens, R., Broadhurst, T., & Illingworth, G. 2003, *ApJ*, 593, 640
Bouwens, R. J., Illingworth, G. D., Franx, M., & Ford, H. 2007, *ApJ*, 670, 928
—, 2008, *ApJ*, 686, 230
Bouwens, R. J., Illingworth, G. D., Oesch, P. A., et al. 2015a, *arXiv:1503.08228*
—, 2012, *ApJ*, 752, L5
—, 2015b, *ApJ*, 803, 34, (B15b)
Bozek, B., Marsh, D. J. E., Silk, J., & Wyse, R. F. G. 2015, *MNRAS*, 450, 209
Bray, H. L., & Goetz, A. S. 2014, *arXiv:1409.7347*
Broadhurst, T. J., Taylor, A. N., & Peacock, J. A. 1995, *ApJ*, 438, 49
Bromm, V., & Yoshida, N. 2011, *ARA&A*, 49, 373
Chavanis, P.-H. 2011, *Phys. Rev. D*, 84, 043531
Chiueh, T. 2014, *arXiv:1409.0380*
Chornock, R., Berger, E., Fox, D. B., et al. 2014, *arXiv:1405.7400*
Coe, D., Bradley, L., & Zitrin, A. 2015, *ApJ*, 800, 84
Coe, D., Zitrin, A., Carrasco, M., et al. 2013, *ApJ*, 762, 32
Cooray, A., & Milosavljević, M. 2005, *ApJ*, 627, L89
Davidson, S. 2015, *Astroparticle Physics*, 65, 101
Diego, J. M., Broadhurst, T., Chen, C., et al. 2015, *arXiv:1504.05953*
Dijkstra, M. 2014, *PASA*, 31, 40
Fan, X., Strauss, M. A., Becker, R. H., et al. 2006, *AJ*, 132, 117
Finkelstein, S. L., Ryan, Jr., R. E., Papovich, C., et al. 2014, *arXiv:1410.5439*
Frye, B., Broadhurst, T., & Benítez, N. 2002, *ApJ*, 568, 558
Gardner, J. P., Mather, J. C., Clampin, M., et al. 2006, *Space Sci. Rev.*, 123, 485
Goodman, J. 2000, *New A*, 5, 103
Guth, A. H., Hertzberg, M. P., & Prescod-Weinstein, C. 2015, *Phys. Rev. D*, 92, 103513
Guzmán, F. S., & Lora-Clavijo, F. D. 2015, *General Relativity and Gravitation*, 47, 21
Hahn, O., & Abel, T. 2011, *MNRAS*, 415, 2101

- Harko, T., & Lobo, F. S. N. 2015, *Phys. Rev. D*, 92, 043011
- Hartoog, O. E., Malesani, D., Fynbo, J. P. U., et al. 2014, arXiv:1409.4804
- Hinshaw, G., et al. 2013, *ApJS*, 208, 19
- Hlozek, R., Grin, D., Marsh, D. J. E., & Ferreira, P. G. 2015, *Phys. Rev. D*, 91, 103512
- Holwerda, B. W., Bouwens, R., Oesch, P., et al. 2015, *ApJ*, 808, 6
- Hu, W., Barkana, R., & Gruzinov, A. 2000, *Phys. Rev. Lett.*, 85, 1158
- Khlopov, M. I., Malomed, B. A., & Zeldovich, I. B. 1985, *MNRAS*, 215, 575
- Khmelnitsky, A., & Rubakov, V. 2014, *J. Cosmology Astropart. Phys.*, 2, 19
- Knollmann, S. R., & Knebe, A. 2009, *ApJS*, 182, 608
- Kuhlen, M., & Faucher-Giguère, C.-A. 2012, *MNRAS*, 423, 862
- Lam, D., Broadhurst, T., Diego, J. M., et al. 2014, *ApJ*, 797, 98
- Lee, J.-W., & Lim, S. 2010, *J. Cosmology Astropart. Phys.*, 1, 7
- Lewis, A., Challinor, A., & Lasenby, A. 2000, *ApJ*, 538, 473
- Lora, V., & Magaña, J. 2014, *J. Cosmology Astropart. Phys.*, 9, 11
- Lovell, M. R., Frenk, C. S., Eke, V. R., et al. 2014, *MNRAS*, 439, 300
- Macciò, A. V., Paduroiu, S., Anderhalden, D., Schneider, A., & Moore, B. 2012, *MNRAS*, 424, 1105
- Madarassy, E. J. M., & Toth, V. T. 2015, *Phys. Rev. D*, 91, 044041
- Marsh, D. J. E. 2015, *Phys. Rev. D*, 91, 123520
- Marsh, D. J. E., & Ferreira, P. G. 2010, *Phys. Rev. D*, 82, 103528
- Marsh, D. J. E., & Pop, A.-R. 2015, *MNRAS*, 451, 2479
- Marsh, D. J. E., & Silk, J. 2014, *MNRAS*, 437, 2652
- Martinez-Medina, L. A., Robles, V. H., & Matos, T. 2015, *Phys. Rev. D*, 91, 023519
- Mason, C., Trenti, M., & Treu, T. 2015, arXiv:1508.01204
- Matos, T., & Arturo Ureña-López, L. 2001, *Phys. Rev. D*, 63, 063506
- McGreer, I. D., Mesinger, A., & D’Odorico, V. 2015, *MNRAS*, 447, 499
- McLeod, D. J., McLure, R. J., Dunlop, J. S., et al. 2015, *MNRAS*, 450, 3032
- McLure, R. J., Dunlop, J. S., Bowler, R. A. A., et al. 2013, *MNRAS*, 432, 2696
- Melandri, A., Bernardini, M. G., D’Avanzo, P., et al. 2015, arXiv:1506.03079
- Mesinger, A., Aykotalp, A., Vanzella, E., et al. 2015, *MNRAS*, 446, 566
- Mielke, E. W., & Pérez, J. A. V. 2009, *Physics Letters B*, 671, 174
- Mitra, S., Choudhury, T. R., & Ferrara, A. 2015, arXiv:1505.05507
- Mocz, P., & Succi, S. 2015, *Phys. Rev. E*, 91, 053304
- Moore, B. 1994, *Nature*, 370, 629
- Oesch, P. A., Bouwens, R. J., Illingworth, G. D., et al. 2014, *ApJ*, 786, 108
- Oesch, P. A., van Dokkum, P. G., Illingworth, G. D., et al. 2015, *ApJ*, 804, L30
- Oke, J. B., & Gunn, J. E. 1983, *ApJ*, 266, 713
- O’Shea, B. W., Wise, J. H., Xu, H., & Norman, M. L. 2015, *ApJ*, 807, L12
- Parsa, S., Dunlop, J. S., McLure, R. J., & Mortlock, A. 2015, arXiv:1507.05629
- Peebles, P. J. E. 2000, *ApJ*, 534, L127
- Pentericci, L., Vanzella, E., Fontana, A., et al. 2014, *ApJ*, 793, 113
- Pieri, M. M., Martel, H., & Grenon, C. 2007, *ApJ*, 658, 36
- Planck Collaboration, Ade, P. A. R., Aghanim, N., et al. 2014, *A&A*, 571, A16
- . 2015, arXiv:1502.01589
- Reddy, N. A., & Steidel, C. C. 2009, *ApJ*, 692, 778
- Rindler-Daller, T., & Shapiro, P. R. 2014, *Mod. Phys. Lett. A*, 29, 1430002
- Robertson, B. E., Ellis, R. S., Furlanetto, S. R., & Dunlop, J. S. 2015, *ApJ*, 802, L19
- Robles, V. H., & Matos, T. 2012, *MNRAS*, 422, 282
- Rodney, S. A., Patel, B., Scolnic, D., et al. 2015, arXiv:1505.06211
- Ruffini, R., & Bonazzola, S. 1969, *Phys. Rev.*, 187, 1767
- Salucci, P., Wilkinson, M. I., Walker, M. G., et al. 2012, *MNRAS*, 420, 2034
- Scannapieco, E., & Broadhurst, T. 2001, *ApJ*, 549, 28
- Schenker, M. A., Ellis, R. S., Konidaris, N. P., & Stark, D. P. 2014, *ApJ*, 795, 20
- Schenker, M. A., Robertson, B. E., Ellis, R. S., et al. 2013, *ApJ*, 768, 196
- Schive, H.-Y., Chiueh, T., & Broadhurst, T. 2014a, *Nat. Phys.*, 10, 496, (SCB14a)
- Schive, H.-Y., Liao, M.-H., Woo, T.-P., et al. 2014b, *Phys. Rev. Lett.*, 113, 261302, (S14b)
- Schneider, A., Anderhalden, D., Macciò, A. V., & Diemand, J. 2014, *MNRAS*, 441, L6
- Schneider, A., Smith, R. E., & Reed, D. 2013, *MNRAS*, 433, 1573
- Schroeder, J., Mesinger, A., & Haiman, Z. 2013, *MNRAS*, 428, 3058
- Schultz, C., Oñorbe, J., Abazajian, K. N., & Bullock, J. S. 2014, *MNRAS*, 442, 1597
- Seidel, E., & Suen, W.-M. 1990, *Phys. Rev. D*, 42, 384
- Sheth, R. K., & Tormen, G. 1999, *MNRAS*, 308, 119, (ST99)
- Sikivie, P., & Yang, Q. 2009, *Phys. Rev. Lett.*, 103, 111301
- Spergel, D. N., Flauger, R., & Hlozek, R. 2015, *Phys. Rev. D*, 91, 023518
- Springel, V. 2005, *MNRAS*, 364, 1105
- Springel, V., & Hernquist, L. 2003, *MNRAS*, 339, 312
- Stadnik, Y. V., & Flambaum, V. V. 2015, arXiv:1506.08364
- Stark, D. P., Richard, J., Charlot, S., et al. 2015, *MNRAS*, 450, 1846
- Steidel, C. C., Pettini, M., & Adelberger, K. L. 2001, *ApJ*, 546, 665
- Strigari, L. E., Bullock, J. S., Kaplinghat, M., et al. 2008, *Nature*, 454, 1096
- Suárez, A., & Matos, T. 2011, *MNRAS*, 416, 87
- Suárez, A., Robles, V. H., & Matos, T. 2014, *Astrophysics and Space Science Proceedings*, 38, 107
- Trakhtenbrot, B., Urry, C. M., Civano, F., et al. 2015, *Science*, 349, 168
- Turner, M. S. 1983, *Phys. Rev. D*, 28, 1243
- Umetsu, K., & Broadhurst, T. 2008, *ApJ*, 684, 177
- Vale, A., & Ostriker, J. P. 2004, *MNRAS*, 353, 189
- Van Tilburg, K., Leefter, N., Bougas, L., & Budker, D. 2015, *Phys. Rev. Lett.*, 115, 011802
- Wang, J., & White, S. D. M. 2007, *MNRAS*, 380, 93
- Widrow, L. M., & Kaiser, N. 1993, *ApJ*, 416, L71
- Wise, J. H., Demchenko, V. G., Halicek, M. T., et al. 2014, *MNRAS*, 442, 2560
- Woo, T.-P., & Chiueh, T. 2009, *ApJ*, 697, 850
- Zheng, W., Postman, M., Zitrin, A., et al. 2012, *Nature*, 489, 406
- Zitrin, A., & Broadhurst, T. 2009, *ApJ*, 703, L132
- Zitrin, A., Zheng, W., Broadhurst, T., et al. 2014, *ApJ*, 793, L12
- Zitrin, A., Labbe, I., Belli, S., et al. 2015, arXiv:1507.02679